AIAA JOURNAL
Vol. 33, No. 6, June 1995

Simulation of Three-Dimensional Turbulent Flows on Unstructured Meshes

Oh Joon Kwon*
NYMA, Inc., Brook Park, Ohio 44142
and
Chunill Hah†
NASA Lewis Research Center, Cleveland, Ohio 44135

A three-dimensional Navier–Stokes flow solver is developed on unstructured tetrahedral meshes. For a turbulence closure, a standard high-Reynolds-number k-ε model with a wall function boundary condition is used. The seven equations of motion are discretized and integrated in a tightly coupled manner. The time integration is achieved using an explicit Runge–Kutta time-stepping scheme. The inviscid flux terms are discretized based on a cell-centered finite volume formulation with Roe's flux-difference splitting. The numerical method is applied for flows on a two-dimensional backward-facing step and a three-dimensional turbomachinery geometry. The results are compared with analytical and experimental data for validations.

Introduction

DESPITE the growing popularity of the unstructured mesh flow calculations, until recently much of this work has been limited to inviscid flow problems.[1–7] Thus the advantage of using unstructured mesh methodology, which provides great flexibility in handling complex configurations, has not fully flourished in solving "real" flows on these geometries where it is needed most. One of the major difficulties in solving viscous flows on unstructured meshes is generating highly stretched, viscous meshes. Recently, progress has been reported in overcoming the difficulty of generating viscous unstructured meshes in two and three dimensions using the advancing-layers method.[8,9]

Another difficulty in developing a viscous unstructured mesh flow solver is in accurately resolving the convective and viscous fluxes on highly stretched triangular/tetrahedral meshes. The degree of difficulty in solving viscous flows tremendously increases in the case of high-Reynolds-number flows. The viscous effect remains inside a very thin layer near the solid surface, which requires an extreme grid stretching. At the same time, a proper turbulence closure is required to model the turbulent viscosity, which results in additional computational effort. The simplest algebraic turbulence model is generally not suitable for random unstructured mesh data structures due to the difficulty of evaluating the distance of each mesh from thenearest wall.

Viscous calculations on unstructured meshes were reported for two-dimensional low-Reynolds-number laminar flows.[10,11] Three-dimensional viscous laminar flow calculations were made using Roe's flux-difference splitting and implicit time integration on a highly stretched unstructured mesh.[12] Until recently, several two-dimensional high-Reynolds-number flow calculations on unstructured meshes were reported using different levels of turbulence closure, such as an algebraic turbulence model using a local structured turbulence mesh,[13,14] a one-equation model,[15] and a two-equation k-ε model.[16,17] Three-dimensional viscous flow calculations with k-ε turbulence equations have been reported using a finite volume method based on central differencing[18,19] and a finite element approach.[20]

In the present paper, a three-dimensional Navier–Stokes flow solver with a k-ε turbulence closure is developed as an extension of a previously validated three-dimensional Euler method.[7,5] The numerical scheme is based on a cell-centered finite volume method with Roe's flux-difference splitting. The flux terms of the turbulence equations are discretized in exactly the same manner as the mean flow equations using flux-difference splitting. The full set of seven governing equations of motion of the mean flow and the turbulence model are integrated in time using a fully explicit Runge–Kutta time stepping in a fully coupled manner using exactly the same time step. Validations are made for a two-dimensional backward-facing step flow to demonstrate the details of the viscous capability of the present method. Three-dimensional applications are made for turbulent viscous flows through typical turbine blades. Comparisons are made with available analytical and experimental results.

Mathematical and Numerical Formulation

Governing Equations

The equations governing three-dimensional, viscous, unsteady, compressible flows are the Reynolds-averaged Navier–Stokes equations that express the conservation of mass, momentum, and energy for a Newtonian fluid in the absence of external forces. The turbulence viscosity is calculated using the standard high-Reynolds-number turbulence model of Launder and Spalding.[21] The seven equations may be written in an integral form for a bounded domain Ω with a boundary $\partial\Omega$:

$$\frac{\partial}{\partial t}\iiint_{\Omega} Q\,\mathrm{d}V + \iint_{\partial\Omega} F(Q)\cdot\hat{n}\,\mathrm{d}S = \iint_{\partial\Omega} G(Q)\cdot\hat{n}\,\mathrm{d}S + \iiint_{\Omega} S(Q)\,\mathrm{d}V \tag{1}$$

where

$$Q = \{\rho, \rho u, \rho v, \rho w, e_0, \rho k.\rho\varepsilon\}^T$$

$F(Q)$ represents the convective flux term and $\hat{n}$ is the exterior surface unit normal vector on the boundary $\partial\Omega$. The Cartesian velocity components are u, v, and w in the x, y, and z directions, respectively. The term e_0 is the total energy per unit volume. The turbulent kinetic energy and the turbulent kinetic energy dissipation rate are represented by k and ε. The viscous heat flux and shear stress vectors are written as

$$G(Q)\cdot\hat{n} = \frac{1}{Re}(\hat{n}_x G_x + \hat{n}_y G_y + \hat{n}_z G_z) \tag{2}$$

Received April 12, 1994; presented as Paper 94-1833 at the AIAA 12th Applied Aerodynamics Conference, Colorado Springs, CO, June 20–23, 1994; revision received Jan. 21, 1995; accepted for publication Jan. 21, 1995.

*Research Engineer, Turbomachinery Analysis Section; currently Assistant Professor, Department of Aerospace Engineering, Korea Advanced Institute of Science and Technology, Taejon, Republic of Korea. Member AIAA.

†Senior Scientist, Internal Fluid Mechanics Division. Member AIAA.

where $\hat{n}_x$, $\hat{n}_y$, and $\hat{n}_z$ are the Cartesian components of the exterior surface unit normal $\hat{n}$. The Prandtl number for air is taken to be 0.72 and the turbulent Prandtl number is 0.9. The laminar viscosity is determined by Sutherland's law. The turbulent viscosity μ_t is computed as

$$\mu_t = C_\mu \rho \frac{k^2}{\varepsilon} Re$$

The source term S contains the production and destruction of turbulent kinetic energy. The source term for the standard high Reynolds number is modeled as

$$S(Q) = \begin{Bmatrix} 0 \\ 0 \\ 0 \\ 0 \\ 0 \\ P - \rho\varepsilon \\ (t_1 P - t_2 \rho\varepsilon)\dfrac{\varepsilon}{k} \end{Bmatrix} \tag{3}$$

The term P represents the production rate of the turbulence kinetic energy, and is defined as

$$P = -\acute{u}\acute{v}\frac{\partial u_i}{\partial x_j}$$

where the Boussinesq approximation is used to model the stress terms

$$-\acute{u}\acute{v} = \mu_t\left[\left(\frac{\partial u_i}{\partial x_j} + \frac{\partial u_j}{\partial x_i}\right) - \frac{2}{3}\frac{\partial u_k}{\partial x_k}\delta_{ij}\right] - \frac{2}{3}\rho k \delta_{ij}$$

The turbulence modeling constants are chosen to be the standard Launder and Spalding[21] values of

$$C_\mu = 0.09, \quad t_1 = 1.44, \quad t_2 = 1.92, \quad \sigma_k = 1.0, \quad \sigma_\varepsilon = 1.3$$

The equations are nondimensionalized with the reservoir flow condition and the reference length. The Reynolds number is calculated based on the reservoir quantities. The molecular and turbulent viscosities are normalized using the molecular viscosity at the reservoir gas state. Equation (1) describes a relationship where the time rate of change to the state vector Q within the domain Ω is balanced by the net flux F and G across the boundary surface $\partial\Omega$. The domain is divided into a finite number of tetrahedral cells, and Eq. (1) is applied to each cell. The state variables Q are volume-averaged values.

Spatial Discretization

The flux across each cell face κ is computed using Roe's flux-difference splitting formula[22]:

$$F_\kappa = \tfrac{1}{2}[F(Q_L) + F(Q_R) - |\tilde{A}|(Q_R - Q_L)]_\kappa \tag{4}$$

where Q_L and Q_R are the state variables to the left and right of the interface κ. The matrix $\tilde{A}$ is computed from evaluating

$$A \equiv \frac{\partial F}{\partial Q}$$

with Roe-averaged quantities as defined in Ref. 23, which includes the turbulent kinetic energy and the turbulent kinetic energy dissipation rate, so that

$$F(Q_R) - F(Q_L) = \tilde{A}[Q_R - Q_L]$$

is satisfied exactly. Introducing the diagonalizing matrices $\tilde{T}$ and $\tilde{T}^{-1}$, and the diagonal matrix of eigenvalues Λ, then $|\tilde{A}|$ is defined as

$$|\tilde{A}| = \tilde{T}|\tilde{\Lambda}|\tilde{T}^{-1}$$

The term

$$|\tilde{A}|(Q_R - Q_L) = \tilde{T}|\tilde{\Lambda}|\tilde{T}^{-1}\Delta Q$$

in Roe's flux formula can be reduced to three ΔF flux components, each of which is associated with a distinct eigenvalue:

$$\tilde{T}|\tilde{\Lambda}|\tilde{T}^{-1}\Delta Q = |\Delta\tilde{F}_1| + |\Delta\tilde{F}_4| + |\Delta\tilde{F}_5| \tag{5}$$

The complete form of the Jacobian matrix, the symmetrization matrices, and the three flux components $|\Delta\tilde{F}_1|$, $|\Delta\tilde{F}_4|$, and $|\Delta\tilde{F}_5|$ are given for the complete set of governing equations in Ref. 23.

For a first-order scheme, the state of the primitive variables at each cell face is set to the cell-centered average on either side of the face. For a higher order scheme, estimation of the state at each cell face is achieved by interpolating the solution at each time step with a Taylor series expansion in the neighborhood of each cell center. The cell-averaged solution gradient required at the cell center for the preceding expansion is computed using Gauss' theorem by evaluating the surface integral for the closed surface of the tetrahedra. This process can be simplified using some geometrical invariant features of the triangles and tetrahedra.[12] The resulting formula for the flow state at each cell face can be written as

$$q_{f_{1,2,3}} = q_i + \tfrac{1}{4}\left[\tfrac{1}{3}(q_{n_1} + q_{n_2} + q_{n_3}) - q_{n_4}\right] \tag{6}$$

where the subscripts n_1, n_2, and n_3 denote the nodes comprising face $f_{1,2,3}$ of cell i and n_4 corresponds to the opposite node. The expansion also requires the nodal value of the solution, which can be computed from the surrounding cell center data using a second-order accurate pseudo-Laplacian averaging procedure as suggested by Homes and Connell.[16] Recently, the three-dimensional extension was made by Frink,[12] which is adopted for the present calculations.

The convective terms of the turbulence equations are calculated using a first-order accurate scheme to reduce the computational cost and to ensure the numerical stability of the time integration[17] in the present paper.

Viscous Fluxes

The evaluation of viscous terms $G(Q)$ requires first derivatives of the velocity, the temperature, and k-ε values at the cell faces. They are achieved by evaluating the gradient of each required flow quantity at the cell center from the known primitive variables at each time step. Applying the gradient theorem gives

$$\nabla\phi_n = \frac{1}{V_\Omega}\oint_{\partial\Omega}\phi\hat{n}\,dS \tag{7}$$

where Ω represents the volume of the domain over which the gradient theorem is applied. The scalar quantity ϕ can be the three components of velocity, the temperature, or turbulence quantities. In the present calculations, the integral domain is defined as the individual tetrahedral cell of the unstructured mesh, which is consistent with the numerical procedure of evaluating the convective fluxes of the present cell-centered scheme. The surrounding surface area $\partial\Omega$ then consists of the four triangular surfaces covering the tetrahedral cell.

For a first-order scheme, the flux through each cell face in Eq. (7) is calculated as an average of the two cell center values of the adjacent cells. Thus, with the known cell volume of V_Ω, the gradient of ϕ can be calculated at each cell center. Then, the cell-averaged viscous shear stresses and heat flux for each tetrahedral cell are calculated at the cell center. The values of G_x, G_y, and G_z at the cell faces for flux calculation in Eq. (1) are determined by the average of the two cell center values of the adjacent cells. The viscous dissipation of the turbulent kinetic energy and the turbulent kinetic energy dissipation rate is calculated in the same manner as described earlier for shear stresses. The turbulent eddy viscosity is evaluated using the cell-averaged values of k and ε.

The second-order approximation of the viscous terms for the mean flow is achieved by using the nodal values of the flow variables calculated using the pseudo-Laplacian averaging described earlier for the convective terms. The flux through each of the triangular faces in Eq. (7) is obtained by the average of the three nodal values for the triangle. Once the gradients of the primitive variables are obtained, the shear stresses and the heat flux can be calculated, from which G_x, G_y, and G_z are evaluated at the cell center. Then,

the nodal values of these quantities are calculated by applying the pseudo-Laplacian averaging on these quantities. The surface flux of these quantities in Eq. (1) is obtained by taking the average of the three nodal values for each triangular face of each cell.

The turbulent production P can be calculated using the first derivative of the three velocity components obtained for viscous shear stresses as described earlier. Then the turbulent source term is calculated at the cell center. The volume integral of the source term in Eq. (1) is calculated by simply multiplying the cell volume to the cell-averaged source term for each tetrahedral cell.

Time Integration

A semidiscrete form of the governing equations reads

$$V_i \frac{\partial Q_i}{\partial t} + R_i = 0, \qquad i = 1, 2, 3, \ldots \tag{8}$$

where

$$R_i = \sum_{j=\kappa(i)} F_{i,j} \Delta S_{i,j}$$

and V_i is the cell volume and R_i is the residual accrued by summation of both the inviscid and viscous fluxes through the four faces κ of a tetrahedral cell i. The source term of the turbulent equations is also included in the residual R_i. The seven equations of motion are integrated in time using a fully explicit m-stage Runge–Kutta time-stepping scheme developed by Jameson et al.[24] in a fully coupled manner based on exactly the same time step for both the mean flow and the turbulence equations. A three-stage scheme was used for the calculations presented in this paper.

The inviscid fluxes are evaluated at each time stage using values of transport variables obtained at the previous stage of the scheme rather than using values from the previous iteration.[25] Meanwhile, in the "uncoupled" procedure, for example, as in Refs. 16 and 26 (sometimes called "lagged" or "split"), the mean flow equations are integrated in time using frozen values of k and ε previously obtained, and the k-ε equations are integrated using the frozen value of the mean flow. The coupled approach gives a more compact and better organized code and is easily extended to unsteady flow calculations. The viscous dissipations and the source terms are evaluated before the first stage and are kept as constants during the time stepping.

To accelerate the convergence of the solution to steady state, local time stepping was used based on a two-dimensional stability analysis.[5] The local time steps are updated at every user-specified number of iterations.

To maximize the time step, an implicit residual smoothing is applied by filtering the residuals through a Laplacian operator for the neighboring cells that share the same faces. This is performed for the odd stage of the Runge–Kutta time cycle by solving the resulting set of equations using Jacobi iteration.[5] Inclusion of the viscous terms in the residual smoothing procedure was essential to obtain a stable and convergent solution. The implicit residual smoothing was also applied to the turbulence equations in exactly the same manner to the mean flow equations.

Unlike some of the explicit time-stepping methods,[17,27] the implicit treatment of the turbulence source terms was not necessary for the present fully coupled solution procedure, which is consistent with the results using structured grids.[25] The addition of turbulence equations did not stiffen the scheme at all using the wall function boundary condition approach.

It is known that the k-ε equations are instability prone during the transitory phase of the computations. To stabilize the computations, k and ε are bounded by the following limiters as suggested in Ref. 27:

$$\begin{aligned} \rho k &\geq K_k \rho_\infty k_\infty > 0 \\ \rho \varepsilon &\geq K_\varepsilon \rho_\infty \varepsilon_\infty > 0 \\ 10P &\geq \rho\varepsilon \geq 0.1P \end{aligned} \tag{9}$$

where $K_\varepsilon = 0.01$–0.0001 and $K_k = 0.0001$ to prevent k and ε from becoming negative.[25] Also, Eq. (9) imposes that the turbulence production at each cell remains in the same order of magnitude as the local turbulent kinetic energy dissipation. $\rho_\infty k_\infty$ and $\rho_\infty \varepsilon_\infty$ are arbitrary reference quantities, taken to be the values at the inlet for the present calculations.

To obtain a stable k-ε behavior at the early stage of computation, it was helpful to integrate the mean flow for a reasonable number of time steps before turning on the turbulence equations. Thus, the mean flow is given a chance to adjust to the flow conditions so that the turbulent production P, which is a function of the mean flow velocity gradients, remains in a reasonable range. This was particularly true for flows with complex geometries involving a large region of reversed flow or high flow turning where a good initial guess of the mean flow was usually unavailable.

Boundary and Initial Conditions

For internal flow calculations, the stagnation pressure, stagnation temperature, and the two inlet flow angles are specified at the inflow boundary. Whenever known, the total pressure and velocity profiles inside the boundary layer on the solid wall are prescribed at the inflow boundary. Other flow quantities are obtained using a characteristic boundary condition by extrapolating the Riemann invariant from the interior of the computational domain. At the flow exit boundary, the static pressure is assumed to be known. Other flow variables such as density and velocities are extrapolated from the inside of the computational domain at the exit plane. The turbulent kinetic energy and the dissipation rate are assumed to be known at the inlet boundary from the known turbulence intensity and the turbulence length scale:

$$k = \tfrac{3}{2}(I_t V)^2$$

$$\varepsilon = k^{\frac{3}{2}}/l$$

where I_t, l, and V represent the turbulence intensity, the turbulent length scale, and the magnitude of total velocity, respectively. At the outflow boundary, the k-ε values are extrapolated.

On the computational boundaries between turbine blades the periodic flow condition is imposed. After each time step, the flow quantities on periodic boundaries are replaced by the cell-centered values and averaged between the two surfaces for each matching triangular element. Then the values are replaced on both boundary surfaces. Since the surface triangular distributions between the two periodic boundaries are constructed to be identical from the grid generation both in number and size, no interpolation of the flow quantities is required to conserve the flow on these boundaries. Information about matching triangles between the two periodic boundary surfaces is predetermined and stored as a preprocessing step before the time integration is performed. The k-ε values are averaged and replaced for the periodic boundaries in a way that is similar to the one performed for the mean flows.

To predict high-Reynolds-number turbulent boundary-layer flows correctly through the laminar, semilaminar, and fully turbulent regions, many grid points are required inside the viscous sublayer (more than 30 points to obtain a reasonably correct value of skin friction[28]) with the near-wall value of $y^+ \simeq 1$. Using the current explicit scheme, three-dimensional flow calculations become very stiff and require an extreme number of iterations on such fine grids, which is not practical even on current supercomputers. To avoid this situation, a semi-empirical wall function boundary condition was imposed on the solid surface for the present turbulent flow calculations.[16,17] It is assumed that the velocity profile between the first grid point (cell center of the first cell adjacent to the solid surface on the present unstructured mesh) and the solid surface obeys the following law of the wall[28]:

$$u^+ = y^+ \qquad \text{for} \qquad y^+ < 11.5 \tag{10}$$

$$u^+ = \frac{1}{\kappa_v} \ell_n(Ey^+) \qquad \text{for} \qquad y^+ > 11.5 \tag{11}$$

where

$$u^+ = \frac{V_a}{u_\tau} \qquad y^+ = \frac{\rho_a y_a u_\tau}{\mu} Re$$

where ρ_a and V_a are the fluid density and the velocity at the cell center of the first cell adjacent to the solid surface at a normal distance y_a away from the surface, u_τ is the friction velocity, κ_v is the von Kármán constant of 0.41, and E is taken to be 9.0 in the present calculation. At each iteration, from the known velocity V_a and y_a, the friction velocity can be calculated using a Newton–Raphson iteration. Then the k and ε at the first cell center point are obtained from the following relations:

$$k = \frac{u_\tau^2}{\sqrt{C_\mu}}$$

$$\varepsilon = \frac{u_\tau^3}{\kappa_v y_a}$$

In practice, when the first cell center point is located very close to the wall, the velocity and the k-ε values at the first cell center can be replaced at the center of the surface triangle. This yields a slip boundary condition rather than a no-slip boundary condition for the mean flow.

On the solid boundaries the velocity gradient normal to the surface is known from the relation between V and y in Eqs. (10) and (11). Thus, the viscous shear stresses on the solid wall are determined and applied as a boundary condition for evaluating the viscous fluxes in Eq. (1). The turbulent viscosity on the solid surface is calculated using the k-ε values on the surface as determined earlier. The first derivatives of k and ε on the solid surface for the turbulence equations are extrapolated from the cell center values of the adjacent tetrahedral cell. For pure laminar flow calculations, a regular no-slip boundary condition is recovered on the solid surface.

The initial condition of the mean flow is assumed to be a uniform flowfield based on the initial guess of the inlet flow. The initial turbulent flowfield is a uniform field based on the inflow k-ε boundary conditions.

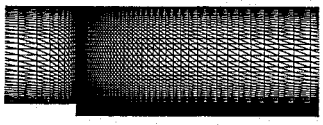

Fig. 1 Stretched triangular mesh for the Driver's backward-facing step flow calculation.

Results and Discussion

The intent to the present work is to provide a validation of the algorithm and the numerical methodology described earlier for calculating three-dimensional viscous fluid flows in tetrahedral meshes. Even though the numerical methodology is developed in three dimensions, it is sometimes easier and clearer to validate the results in two dimensions where well-defined analytical and experimental data are available. The capability of the present methodology of calculating viscous terms was previously demonstrated for a flat-plate laminar boundary-layer flow.[29] In the present paper the k-ε equations are validated for a well-known backward-facing step flow, where not only the mean flow but also detailed turbulent kinetic energy and turbulent shear stress distributions are available. A three-dimensional calculation is demonstrated for a turbulent flow through typical turbine blades. Viscous unstructured meshes are obtained by dividing structured grids into tetrahedral meshes to obtain the proper grid density and stretching in the direction normal to the solid surface. The viscous calculations are performed with a Courant–Friedrichs–Lewy (CFL) number of 2. The local time step is evaluated for every 20 iterations. Turbulent flow calculations using the higher order scheme require approximately 19 μs of Cray-C90 time per cell per iteration.

Two-Dimensional Turbulent Backward-Facing Step Flow

The backward-facing step flow has been frequently used to benchmark turbulent models. In the present study, the experiment of Driver and Seegmiller[30] has been chosen because the measurement includes details of the mean flow velocity profile, the turbulent kinetic energy, the shear stress, the skin friction, and the pressure distributions. Two-dimensional simulations using the present three-dimensional solver were made on three-dimensional meshes that were composed of three structured two-dimensional grid planes of the same size and shape allocated parallel in the direction normal to the flow plane. The two-dimensional grids were connected each other and divided into tetrahedral meshes. The two outer planes were treated as periodic boundaries, and the derivatives normal to these planes were set to zero to simulate pure two-dimensional flows. The results

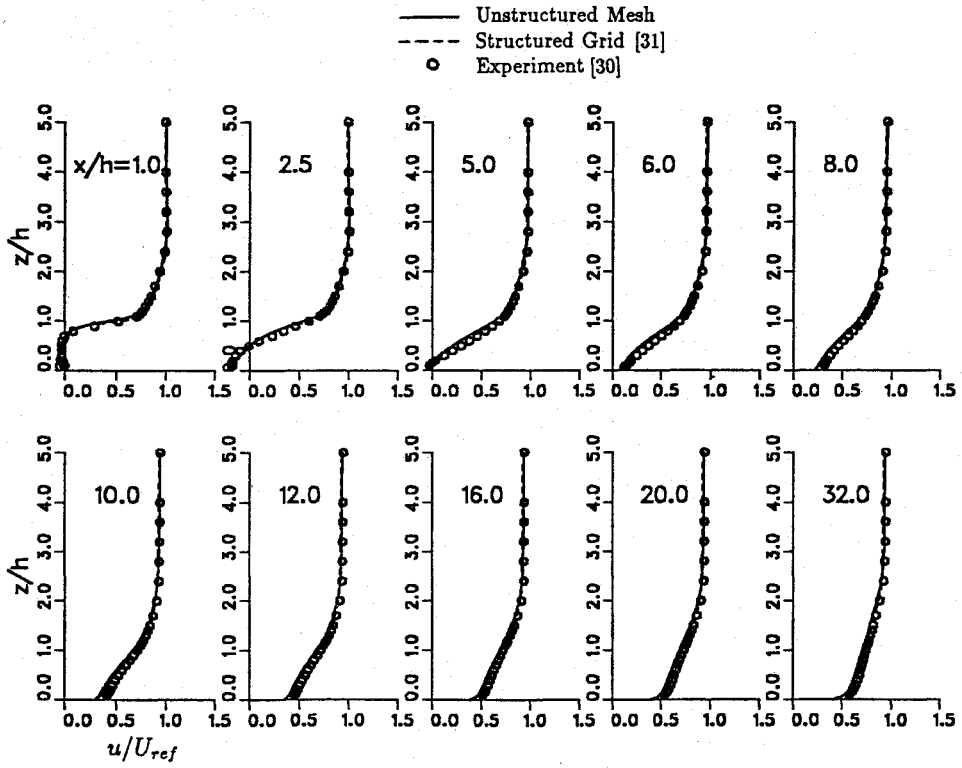

Fig. 2 Comparison of the mean velocity profiles downstream of the step.

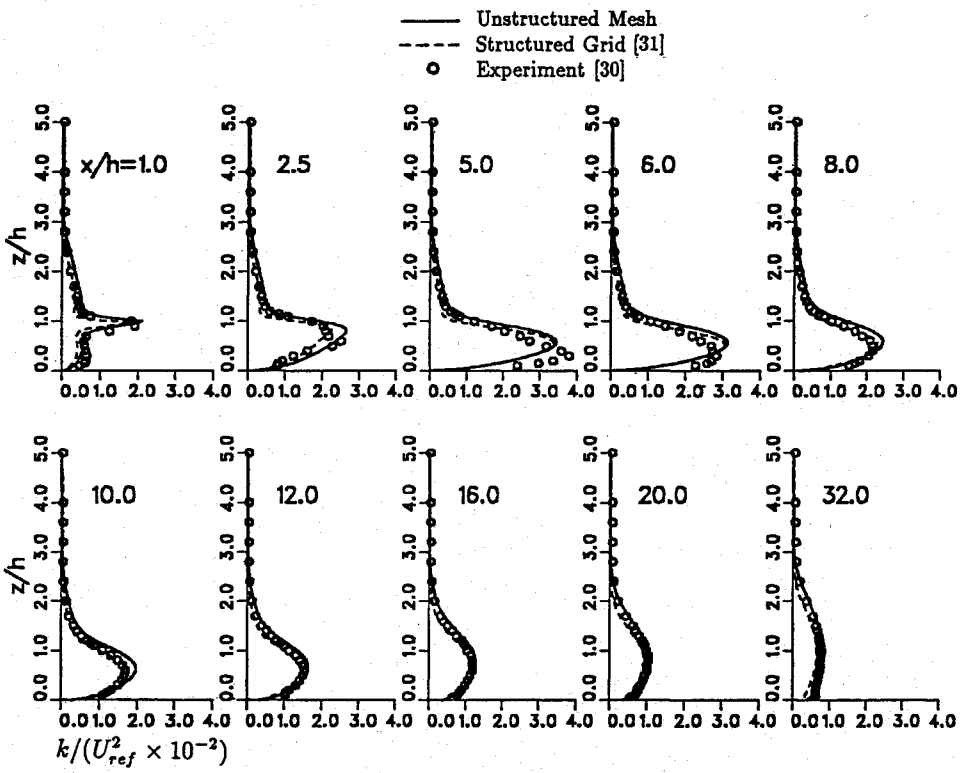

Fig. 3 Comparison of the turbulent kinetic energy profiles downstream of the step.

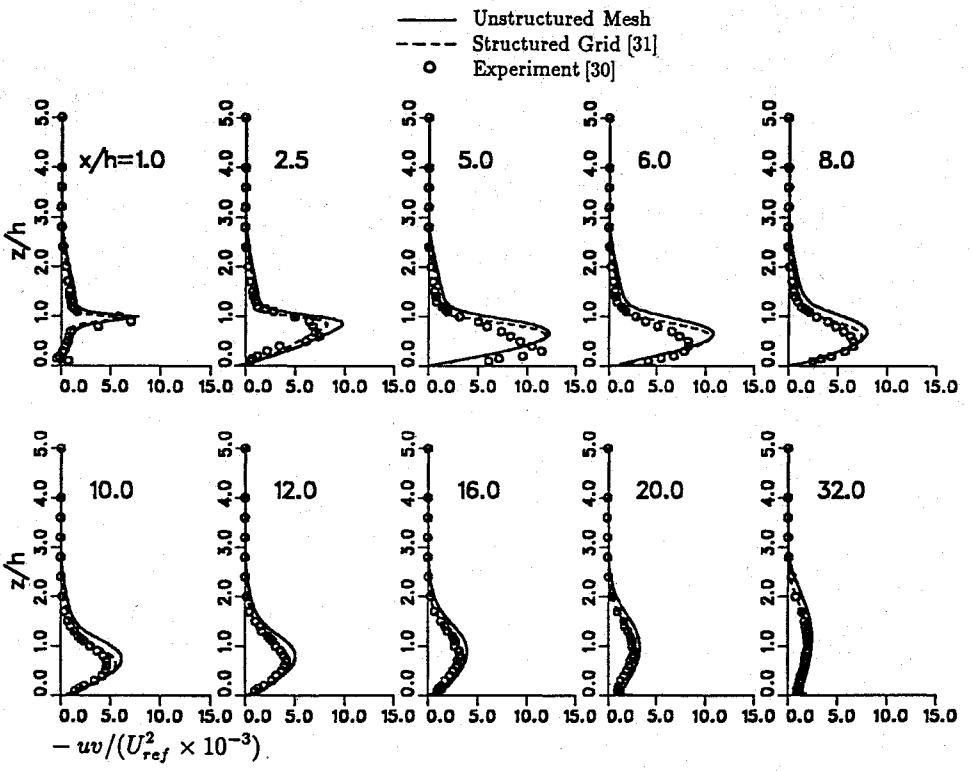

Fig. 4 Comparison of the turbulent shear stress profiles downstream of the step.

are compared with the experiment and the existing structured grid results using a standard high-Reynolds-number turbulence model with a wall function boundary condition.[31] The inlet of the experiment was located 80 step height lengths upstream of the step. The downstream exit was located 60 step height lengths downstream of the step. The expansion ratio (the ratio of downstream channel height to upstream channel height) was 1.125 (for the zero deflection angle case). The inlet Mach number (U_{ref}) was 0.128 and the Reynolds number based on the step height and the inlet velocity was 3.342×10^4.

The numerical domain extended 15 step height lengths upstream of the step. The downstream was stretched up to 60 step height lengths. A partial view of the grid is shown in Fig. 1 near the expansion area. The mesh contains 8720 triangular elements in the two-dimensional plane, which was obtained from three blocks of the structured grid of the size by 14×41, 65×41, and 21×65. In

the direction normal to the flow plane, three grid points were allocated for three-dimensional calculations as described earlier, which produces a total of 52,320 tetrahedral cells. The first cell center point was located at 0.0125 step height lengths away from the solid surface, which yielded a y^+ value of 10–17 in the attached flow region.

The mean flow velocity profiles are shown in Fig. 2 and compared with both the experiment and the structured grid results at 10 different streamwise stations downstream of the step. Excellent correlations are observed for all streamwise stations. The present calculation shows almost identical velocity profiles with the structured grid results.

In Figs. 3 and 4, the turbulent kinetic energy and the turbulent shear stress distributions are compared with the experiment and the results from the structured grid calculation. In the neighborhood of reattachment, the location of the peak values was predicted slightly away from the experiment. A similar behavior is also shown in the structured grid results. This discrepancy is probably due to the characteristics of the k-ε model rather than the numerical method used. In the region downstream of the reattachment, the present unstructured mesh calculation predicts slightly higher values of turbulent quantities than the structured grid results, which could be the effect of grid density (the structured grid calculation was performed on about twice as many grid points as the present unstructured mesh calculation).

The wall static pressure coefficient for both the step-side wall and the opposite wall are shown in Fig. 5. The pressure coefficient was calculated based on the pressure at 6.5 step height lengths upstream of the step and the inlet velocity. Calculation for the step-side wall shows the premature pressure rise by the present k-ε model. A similar trend was also noticed in the results based on the structured grid.[30,31] The minimum and maximum values of the pressure and the steep pressure gradient in the vicinity of reattachment are reasonably well predicted. The pressure recovery downstream of the reattachment is slightly overpredicted by the present calculation, which is consistent with the results obtained using the structured grids. The skin-friction coefficients are shown in Fig. 6. The level of skin friction inside the reversed flow region and after the flow reattachment is well predicted using the wall function boundary condition.

The predicted flow reattachment was about 5.2 step height lengths downstream from the step, which is about 15% less than the experimentally measured value of 6.1. The predicted reattachment points reported, which were based on the structured grid calculations, were about 5.5 in Ref. 31 and 5.2 in Ref. 28.

Three-Dimensional Turbulent Flow Through Turbine Blades

A three-dimensional turbulent flow was calculated for a typical turbine annular cascade where well-documented experimental data are available.[32,33] The full geometry consists of an annular ring of 36 core turbine stator vanes. The geometry is a 38.10-mm-high untwisted blade of constant profile with an axial chord of 38.23 mm. The stator has a tip diameter of 508 mm and a 0.84 hub-to-tip radius ratio.

The calculation was performed for the design flow condition. At the inlet the total temperature and the total pressure profile inside the boundary layer were known from the experiment. The inlet flow angle was zero (flow parallel to the axis of the full cascade). The calculation was made for a static-to-inlet total pressure ratio of 0.665 on the hub of the flow exit plane. The Reynolds number based on the inlet total quantities and the axial chord length was 898,650.

Figure 7 shows the computational domain and the surface triangulation on the hub and the blade surfaces. The tetrahedral mesh for the present calculation was obtained from a structured grid of $77 \times 25 \times 22$, which yields a total of 229,824 cells. The first cell center point was located at approximately 0.0011 axial chord length away from the solid surface, with gives a value of y^+ between 5 and 34. The computational domain was extended one-half axial chord length upstream of the blade leading edge and one axial chord length downstream of the blade trailing edge.

The actual computation was divided into two steps to reduce the computational time. Initially the first 2000 time iterations were performed using the less expensive inviscid Euler calculation with a higher CFL number of 3. During this inviscid calculation, the overall mean flow characteristics through the turbine blade passages were approximately developed for the given inlet and exit flow conditions starting from the crude initial distribution of uniform flow. Then, the full viscous turbulence calculation was restarted from the previous inviscid solution. The convergence history of the rms of the residual of both the mean flow and the turbulence quantities is shown in Fig. 8 as a function of the time iterations. No attempt was made

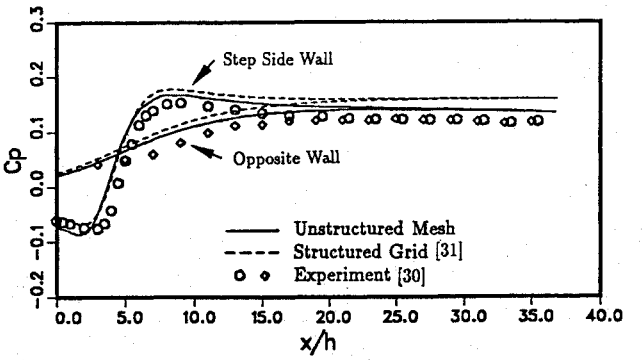

Fig. 5 Wall static pressure coefficient downstream of the step.

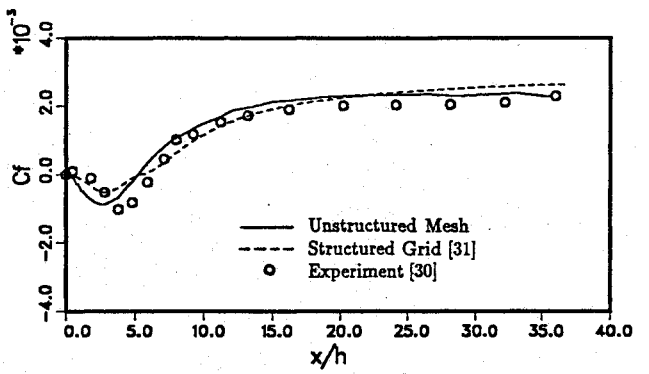

Fig. 6 Wall skin-friction coefficient downstream of the step.

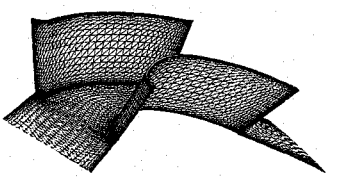

Fig. 7 Surface triangulation of the computational domain for the three-dimensional annular cascade.

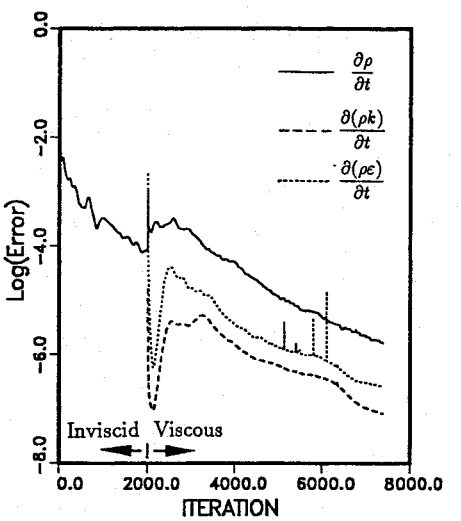

Fig. 8 Convergence rate of density and k-ε equations for the turbine blade calculation.

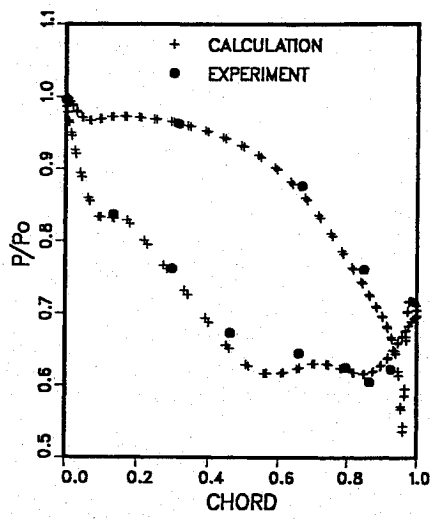

Fig. 9 Static pressure distribution on the blade at 13.3% span.

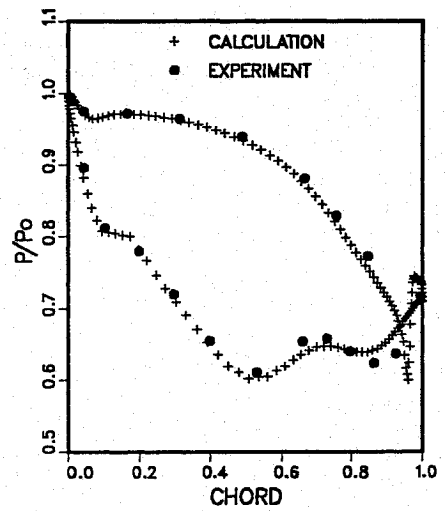

Fig. 10 Static pressure distribution on the blade at 50.0% span.

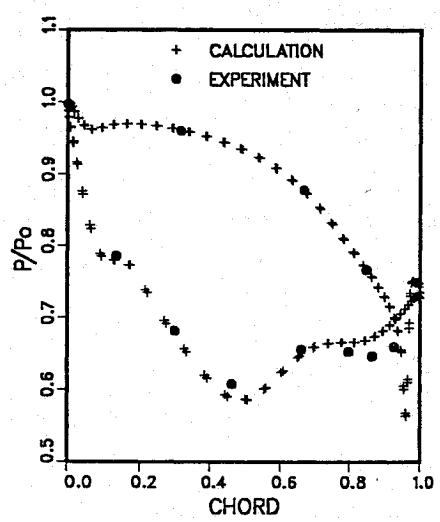

Fig. 11 Static pressure distribution on the blade at 86.7% span.

to determine an optimum number of inviscid time iterations in the present calculation.

The resulting flowfield is fully subsonic. The surface pressure distributions are compared with the experiment at three spanwise stations. In Figs. 9–11 the chordwise surface static pressures normalized by the inlet total pressure are compared with the experiment at 13.3, 50, and 86.7% radial stations. The comparison

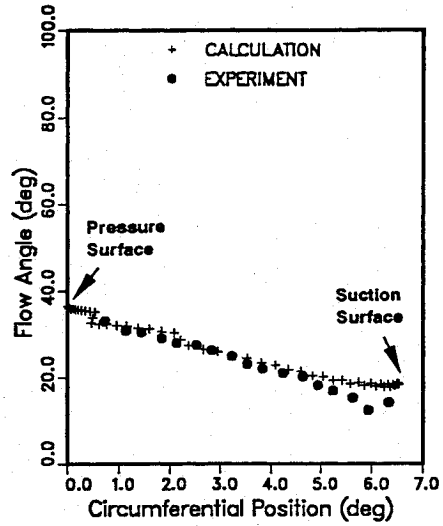

Fig. 12 Flow angle at 30% of axial chord and 50% of span.

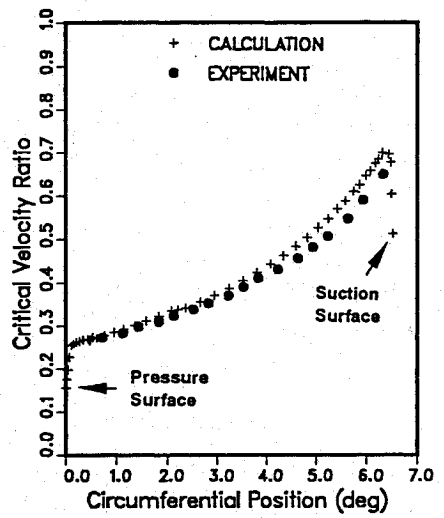

Fig. 13 Critical velocity ratio at 30% of axial chord and 50% of span.

shows that the overall performance of the cascade blade is reasonably well predicted. The predicted pressure on the suction side of the blade near the trailing edge is slightly higher than the experiment.

The flow angle and the critical velocity ratio (local Mach number) within the passage are compared with the experiment, which was obtained using the laser survey measurements at 30% axial chord of the blade at 50% of the span as a function of circumferential position between the blade surfaces. The flow angle was defined by the angle between the axial velocity component and the circumferential velocity component. Figure 12 shows the comparison of the flow angle between the present calculation and the experiment. Even though the predicted flow angle near the suction surface is slightly higher than the measurement, the overall agreement between the experiment and the calculation is considered to be very good. The critical velocity ratio comparison in Fig. 13 also shows good agreement between the prediction and the measurement. Similar comparisons between the calculation and the experiment are made at 70% axial chord at 50% of the span in Figs. 14 and 15.

The aftermixed flow angle and the total pressure loss (defined as a deficiency of the exit-to-inlet total pressure ratio) are compared with the experiment in Figs. 16 and 17. The measurement was taken at approximately one-third axial chord length downstream from the vane trailing edge to obtain the aftermixed conditions, where the flow was assumed to be at circumferentially uniform conditions.[32] The calculated values were obtained by averaging the circumferential variation of the flow at each radial position. The calculated aftermixed flow angle compares well with the experiment, even

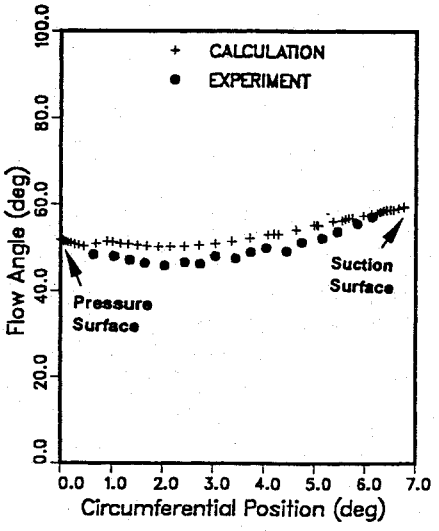

Fig. 14 Flow angle at 70% axial chord and 50% of span.

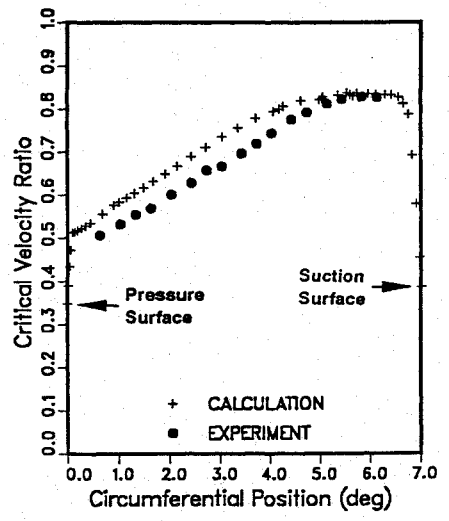

Fig. 15 Critical velocity ratio at 70% of axial chord and 50% of span.

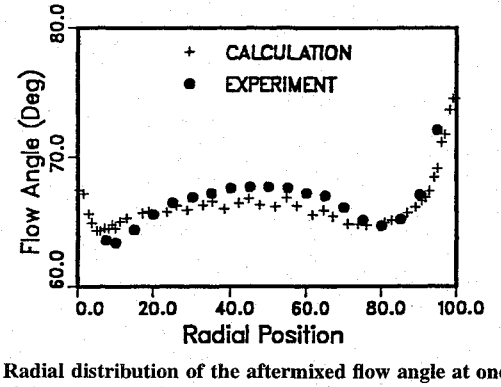

Fig. 16 Radial distribution of the aftermixed flow angle at one-third axial chord downstream of the blade.

though the calculation shows less radial variation than the experiment. The high flow angle near the hub and the shroud due to the endwall crossflow from pressure to suction surface is well predicted. The design flow angle was 67 deg.

In Fig. 17, the aftermixed total pressure loss is compared with the measurement. Even though the predicted loss is slightly higher than the measurement, the overall loss profile is well predicted. The high loss near the end wall due to the boundary layer is also well predicted, which demonstrates the ability of the present scheme to solve viscous calculations.

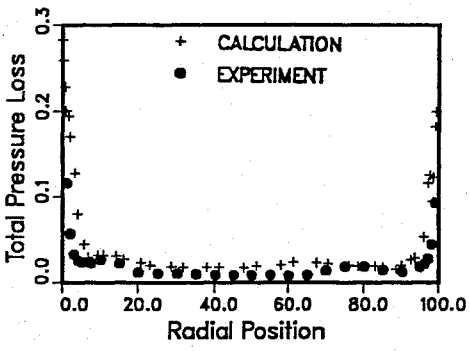

Fig. 17 Radial distribution of the aftermixed total pressure loss coefficient at one-third axial chord downstream of the blade.

Conclusion

A three-dimensional unstructured mesh Navier–Stokes flow solver is developed with k-ε turbulence closure. The scheme is based on explicit Runge–Kutta time stepping with cell-centered finite volume flux-difference splitting. The turbulence equations are discretized and integrated in a fully coupled manner with the mean flow equations. The turbulence equations are validated for a two-dimensional backward-facing step flow. The mean flow, turbulence kinetic energy, and turbulent shear stress profiles for several streamwise stations compare very well with the experiment. The wall static pressure and skin friction are also well predicted within the accuracy of the present turbulence model. A three-dimensional application was made for a turbulent flow through typical turbine blades. The blade surface pressures, the flow angle, and the velocity magnitude inside the flow passage are well predicted. The total pressure loss due to the viscosity is also well predicted.

Acknowledgments

The authors would like to express their indebtedness to Neal T. Frink at NASA Langley for his help and encouragement during the course of the present work. Chris J. Steffen at NASA Lewis is also appreciated for technical discussions and for providing experimental data and structured grid results for the backward-facing step flow.

References

[1]Frink, N. T., Parikh, P., and Pirzadeh, S., "A Fast Upwind Solver for the Euler Equations on Three-Dimensional Unstructured Meshes," AIAA Paper 91-0102, Jan. 1991.

[2]Barth, T. J., "A 3-D Upwind Euler Solver for Unstructured Meshes," AIAA Paper 91-1548, June 1991.

[3]Frink, N. T., Parikh, P., and Pirzadeh, S., "Aerodynamic Analysis of Complex Configurations Using Unstructured Grids," AIAA Paper 91-3292, Sept. 1991.

[4]Batina, J. T., "A Fast Implicit Upwind Solution Algorithm for Three-Dimensional Unstructured Dynamic Meshes," AIAA Paper 92-0447, Jan. 1992.

[5]Frink, N. T., "Upwind Scheme for Solving the Euler Equations on Unstructured Tetrahedral Meshes," *AIAA Journal*, Vol. 30, No. 1, 1992, pp. 70–77.

[6]Mavriplis, D. J., "Three-Dimensional Unstructured Multigrid for the Euler Equations," *AIAA Journal*, Vol. 30, No. 7, 1992, pp. 1753–1761.

[7]Kwon, O, J., and Hah, C., "Three-Dimensional Unstructured Grid Euler Method Applied to Turbine Blades," AIAA Paper 93-0196, Jan. 1993.

[8]Pirzadeh, S., "Unstructured Viscous Grid Generation by Advancing-Layers Method," AIAA Paper 93-3453, Jan. 1993.

[9]Pirzadeh, S., "Viscous Unstructured Three-Dimensional Grids by the Advancing-Layers Method," AIAA Paper 94-0417, Jan. 1994.

[10]Mavriplis, M. J., "Multigrid Solution of the Navier–Stokes Equations on Triangular Meshes," NASA CR-181786, Feb. 1989.

[11]Hwang, C. J., and Liu, J. L., "Inviscid and Viscous Solutions for Airfoil/Cascade Flows Using a Locally Implicit Algorithm on Adaptive Meshes," American Society of Mechanical Engineers, ASME Paper 90-GT-262, Brussels, Belgium, June 1990.

[12]Frink, N. T., "Recent Progress Toward a Three-Dimensional Unstructured Navier–Stokes Flow Solver," AIAA Paper 94-0061, Jan. 1994.

[13]Mavriplis, D. J., "Algebraic Turbulence Modeling for Unstructured and Adaptive Meshes," AIAA Paper 90-1653, June 1990.

[14]Pan, D., and Cheng, J.-C., "Upwind Finite-Volume Navier–Stokes Computations on Unstructured Triangular Meshes," *AIAA Journal*, Vol. 31, No. 9, 1993, pp. 1618–1625.

[15]Barth, T. J., "Numerical Aspects of Computing Viscous High Reynolds Number Flows on Unstructured Meshes," AIAA Paper 91-0721, Jan. 1991.

[16]Holmes, D. G., and Connell, S. D., "Solution of the 2D Navier–Stokes Equations on Unstructured Adaptive Grids," AIAA Paper 89-1932, June 1989.

[17]Mavriplis, D. J., "Multigrid Solution of Compressible Turbulent Flow on Unstructured Meshes Using a Two-Equation Model," AIAA Paper 91-0237, Jan. 1991.

[18]Dawes, W. N., "The Simulation of Three-Dimensional Viscous Flow in Turbomachinery Geometries Using a Solution-Adaptive Unstructured Mesh Methodology," American Society of Mechanical Engineers, ASME Paper 91-GT-124, Orlando, FL, June 1991.

[19]Spragle, G. S., Smith, W. A., and Yadlin, Y., "Application of an Unstructured Flow Solver to Planes, Trains and Automobiles," AIAA Paper 93-0889, Jan. 1993.

[20]Marcum, D. L., and Agarwal, R. K., "A Three-Dimensional Finite Element Navier–Stokes Solver with k-ε Model for Unstructured Grids," AIAA Paper 90-1652, June 1990.

[21]Launder, B. E., and Spalding, D. B., "The Numerical Computation of Turbulent Flows," *Computer Methods in Applied Mechanics and Engineering*, Vol. 3, 1974, pp. 269–289.

[22]Roe, P. L., "Characteristic-Based Schemes for the Euler Equations," *Annual Review of Fluid Mechanics*, Vol. 18, 1986, pp. 337–365.

[23]Morrison, J., "Flux Difference Split Scheme for Turbulent Transport Equations," AIAA Paper 90-5251, Oct. 1990.

[24]Jameson, A., Schmidt, W., and Turkel, E., "Numerical Solution of the Euler Equations by Finite-Volume Methods Using Runge–Kutta Time-Stepping Schemes," AIAA Paper 81-1259, June 1981.

[25]Kunz, R. F., and Lakshminarayana, B., "Stability of Explicit Navier–Stokes Procedures Using k-ε and k-ε/Algebraic Reynolds Stress Turbulence Models," *Journal of Computational Physics*, Vol. 103, No. 1, 1992, pp. 141–159.

[26]Jennions, I. K., and Turner, M. G., "Three-Dimensional Navier–Stokes Computations of Transonic Fan Flow Using an Explicit Flow Solver and an Implicit k-ε Solver," American Society of Mechanical Engineers, ASME Paper 92-GT-309, Cologne, Germany, June 1992.

[27]Gerolymos, G. A., "Implicit Multiple-Grid Solution of the Compressible Navier–Stokes Equations Using k-ε Turbulence Closure," *AIAA Journal*, Vol. 28, No. 10, 1990, pp. 1707–1717.

[28]Avva, R. K., Smith, C. E., and Singhal, A. K., "Comparative Study of High and Low Reynolds Number Versions of k-ε Models," AIAA Paper 90-0246, Jan. 1990.

[29]Kwon, O. J., and Hah, C., "Solution of the 3-D Navier–Stokes Equations with a Two-Equation Turbulence Model on Unstructured Meshes Applied to Turbomachinery," AIAA Paper 94-1833, Jan. 1994.

[30]Driver, D. M., and Seegmiller, H. L., "Features of a Reattaching Turbulent Shear Layer in Divergent Channel Flow," *AIAA Journal*, Vol. 30, No. 5, 1992, pp. 1314–1320.

[31]Steffen, C. J., Jr., "A Critical Comparison of Several Low Reynolds Number k-ε Turbulence Models for Flow Over a Backward-Facing Step," AIAA Paper 93-1927, June 1993.

[32]Goldman, L. J., and McLallin, K. L., "Cold-Air Annular-Cascade Investigation of Aerodynamic Performance of Core-Engine-Cooled Turbine Vanes. I—Solid-Vane Performance and Facility Description," NASA TM X-3224, April 1975.

[33]Goldman, L. J., and Seasholtz, R. G., "Laser Anemometer Measurements in an Annular Cascade of Core Turbine Vanes and Comparison with Theory," NASA TP-2018, June 1982.